Periodic venting of MABR lumen allows high removal rates and high gas-transfer efficiencies

Perez-Calleja, P; Aybar, M; Picioreanu, C.; Esteban-Garcia, A. L.; Martin, K. J.; Nerenberg, R

DOI
10.1016/j.watres.2017.05.042

Publication date
2017

Document Version
Final published version

Published in
Water Research

Water Research 121 (2017) 349–360

Contents lists available at ScienceDirect

Water Research

journal homepage: www.elsevier.com/locate/watres

Periodic venting of MABR lumen allows high removal rates and high gas-transfer efficiencies

P. Perez-Calleja [a, b], M. Aybar [a, c], C. Picioreanu [d], A.L. Esteban-Garcia [b], K.J. Martin [e], R. Nerenberg [a, *]

[a] University of Notre Dame, Department of Civil and Environmental Engineering and Earth Sciences 156 Fitzpatrick Hall, Notre Dame, IN, 46556, USA
[b] University of Cantabria, Department of Sciences and Techniques of Water and the Environment, University of Cantabria, Avda. Los Castros s/n, 39005, Santander, Spain
[c] Department of Civil Engineering, University of Concepcion, Casilla 160-C, Ciudad Universitaria, Concepcion, Chile
[d] Department of Biotechnology, Faculty of Applied Sciences, Delft University of Technology, Van der Maasweg 9, 2629 HZ, Delft, The Netherlands
[e] Black and Veatch, 8400 Ward Parkway, Kansas City, MO, 64114, USA

ARTICLE INFO

Article history:
Received 8 December 2016
Received in revised form
19 April 2017
Accepted 20 May 2017
Available online 22 May 2017

Keywords:
Hollow-fiber membranes
MBfR
MABR
Gas back-diffusion
Gas transfer efficiency
Gas transfer rate

ABSTRACT

The membrane-aerated biofilm reactor (MABR) is a novel treatment technology that employs gas-supplying membranes to deliver oxygen directly to a biofilm growing on the membrane surface. When operated with closed-end membranes, the MABR provides 100-percent oxygen transfer efficiencies (OTE), resulting in significant energy savings. However, closed-end MABRs are more sensitive to back-diffusion of inert gases, such as nitrogen. Back-diffusion reduces the average oxygen transfer rates (OTR), consequently decreasing the average contaminant removal fluxes (J). We hypothesized that venting the membrane lumen periodically would increase the OTR and J. Using an experimental flow cell and mathematical modeling, we showed that back-diffusion gas profiles developed over relatively long timescales. Thus, very short ventings could re-establish uniform gas profiles for relatively long time periods. Using modeling, we systematically explored the effect of the venting interval (time between ventings). At moderate venting intervals, opening the membrane for 20 s every 30 min, the venting significantly increased the average OTR and J without substantially impacting the OTEs. When the interval was short enough, in this case shorter than 20 min, the OTR was actually higher than for continuous open-end operation. Our results show that periodic venting is a promising strategy to combine the advantages of open-end and closed end operation, maximizing both the OTR and OTE.

1. Introduction

Gas-transferring, hollow-fiber membranes (HFM) are commonly used to supply gases for environmental, industrial and medical applications. For example, bundles of HFMs have been used for oxygenation of rivers and water streams, for blood oxygenation, and for bioremediation of groundwater contaminants (Weiss et al., 1998; Roggy et al., 2002; Federspiel and Henchir, 2004). However, an emerging application is the membrane-biofilm reactor (MBfR), where HFMs supply gaseous substrates to a biofilm growing directly on the membrane's outer surface (Martin and Nerenberg, 2012; Nerenberg, 2016). When used to deliver air or oxygen, the process is often referred to as the membrane-aerated biofilm reactor (MABR). MABRs can simultaneously remove biological oxygen demand (BOD), nitrify, and denitrify (Downing and Nerenberg, 2008; Timberlake et al., 1988; Hibiya et al., 2003; Semmens et al., 2003; Terada et al., 2003; Jácome et al., 2006; Matsumoto et al., 2007; Syron and Casey, 2008). Several commercial applications are in development, but very few full-scale applications exist.

MABRs can be operated with closed or open-ended HFMs. With closed-ended HFMs, all the oxygen supplied to the membranes is delivered to the biofilm, allowing 100% oxygen transfer efficiencies (OTEs) (Brindle et al., 1998; Pankhania et al., 1999; Hibiya et al., 2003; Terada et al., 2003; Syron and Casey, 2008; Martin and Nerenberg, 2012). This can save up to 85% in energy costs,

* Corresponding author.
E-mail addresses: pperezca@nd.edu (P. Perez-Calleja), maybar@nd.edu, maybar@udec.cl (M. Aybar), c.picioreanu@tudelf.nl (C. Picioreanu), analorena.esteban@unican.es (A.L. Esteban-Garcia), MartinKJ@bv.com (K.J. Martin), nerenberg.1@nd.edu (R. Nerenberg).

http://dx.doi.org/10.1016/j.watres.2017.05.042
0043-1354/

Abbreviations

DO	Dissolved oxygen
GTE	Gas transfer efficiency
GTR	Gas transfer rate
J	Contaminant removal flux
HFM	Hollow-fiber membrane
MABR	Membrane-aerated biofilm reactor
MBfR	Membrane-biofilm reactor

compared to conventional activated sludge process (Aybar et al., 2014). However, closed-ended HFMs typically suffer from gas back-diffusion, where N_2 and other dissolved gases diffuse into the membrane lumen (Schaffer et al., 1960; Ahmed and Semmens, 1992a). With back-diffusion, the distal end of the membrane may be "deadened," leading to lower average oxygen transfer rates (OTR) compared to open-end operation (Fig. 1a). In this paper, we consider OTR to be synonymous with the oxygen flux, J_{O2}, across the membrane.

With open-ended HFMs, the intra-membrane gas velocity is high throughout the membrane. With high velocities, advective mass transport in the lumen is much greater than the diffusive transfer across the membrane wall. This results in more uniform oxygen concentrations in the lumen, leading to high average OTRs (Fig. 1b). However, a large amount of gas is lost from open end. Also, the high gas velocity leads to greater frictional pressure losses occurrence along the membrane, resulting in greater energy requirements and lower gas pressures at the distal end of the membrane. For the MABR, lower overall OTR translates into lower average substrate removal fluxes (J).

Many researchers have explored ways to improve the OTR of HFMs (Weissman and Mockros, 1969; Tanishita et al., 1978; Côte et al., 1989; Ahmed and Semmens, 1992b; Matsuda et al., 1999; Ahmed et al., 2004). However, few studies have tried to concurrently improve the OTR and OTE. A novel approach may be periodically opening the membranes to vent back-diffusion gases. This will allow the back-diffusion gases to be vented to the atmosphere during the open phase, re-establishing the uniform almost constant gas pressure profile along the fiber length.

Previous research experimentally explored increasing the gas flow rates, or intermittent degassing processes (Li et al., 2010; Castagna et al., 2015). Fang et al. (2004) measured and modeled the gas composition inside a membrane, and gave modeled predictions of gas concentration profiles as a function of time applying when supplied with a pulsing strategy. However, they did not systematically explore the impacts of the pulsing frequency on the OTE and OTR, and their model was only applicable under conditions of liquid creeping flow.

The objective of this study was to use experiments and modeling to systematically explore periodic venting of hollow-fiber membranes as a means to maximize the OTE and OTR of MABRs.

2. Materials and methods

Our strategy was to (1) experimentally study OTRs and OTEs for "clean" HFMs (i.e., without biofilm), for open end, closed end, and for periodic venting, (2) use mathematical modeling to expand the experimental findings and predict the effects of periodic venting for a clean HFM, and (3) experimentally assess the periodic venting strategy for an MABR (i.e., a HFM with biofilm). OTR was calculated as the oxygen flux difference between the inlet and the outlet which corresponds to the flux of oxygen transferred across the membrane surface. OTE was calculated as the flux difference divided by the inlet flux. OTE represents the percentage of the transferred oxygen flux with respect to the supplied oxygen. Fluxes were estimated according to equation (1).

2.1. Experimental flow cells configuration

An experimental flow cell with a single HFM was used to explore OTRs and gas back diffusion in clean HFMs, i.e., without biofilm. The flow cell consisted of square-section glass tube with 6-mm inside dimension, and 40-cm length. The flow cell had seven ports for dissolved oxygen (DO) measurements (Fig. 2), separated 3.8 cm along the flow cell. Water was deoxygenated by nitrogen sparging and pumped through the flow cell using a peristaltic pump (Cole Palmer, Vernon Hills, IL, USA).

Tests were first carried out to determine the HFM's mass transfer coefficient. To test the mathematical model, experiments were then performed with a range of water velocities, oxygen supply pressures, feed gases (air and pure oxygen), water flow directions (co-current or counter current with respect to the inlet gas supply), and transient shifts between open and closed ends.

The flow cell used a composite, microporous polyethylene membrane with a dense 1 μm polyurethane core (HFM200TL, Mitsubishi Rayon, Japan). The outer diameter was 280-μm and the wall thickness was 40-μm. A single membrane was located in the middle of the flow cell, supported at both ends by a gas-supplying manifold. The gas was supplied from one end at constant pressure,

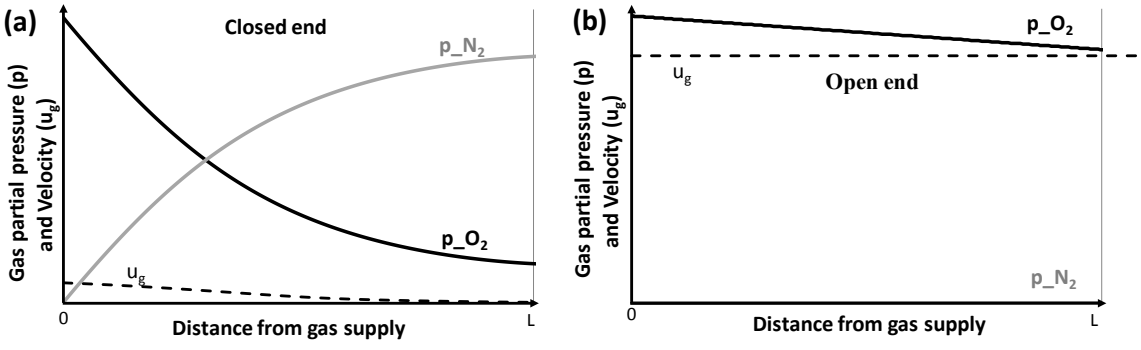

Fig. 1. Schematic showing differences between hollow-fiber membranes at steady-state in: (a) closed-end operation, and (b) open-end operation. In this example, the membrane is pressurized with pure O_2 transferring to liquid containing dissolved N_2. Figures show typical oxygen and nitrogen partial pressures (p_{O2} and p_{N2}) and gas velocities (u_g) along the membrane length. The open end membrane has higher p_{O2} across the entire membrane, leading to higher gas transfer rates, but has low gas transfer efficiencies, as most of the gas is vented through the end.

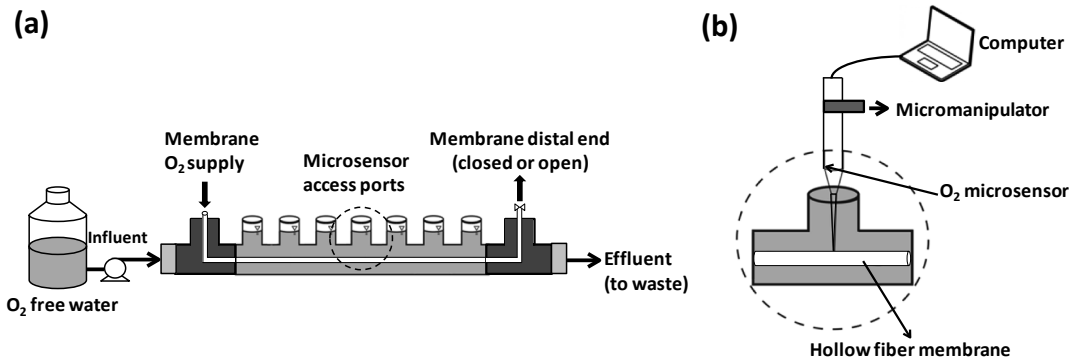

Fig. 2. (a) Schematic of flow cell. Oxygen-free water from a reservoir was pumped into the square-section glass tube with a hollow-fiber membrane supplied with O_2 or air in the middle. (b) Detail of a flow-cell port used for DO measurement with a microsensor controlled by a micromanipulator.

while a valve at the opposite end allowed open or closed operation of the membrane. Pure oxygen or air was supplied at 0.07 or 0.18 atm relative pressure. The influent flow rate ranged from 2 to 10 mL/min, resulting in a liquid velocity of 1–5 mm/s and a Reynolds number of 5–28, well within the laminar flow regime.

Two separate reactors were used for the MABR tests, with the same configuration as described above. Reactor MABR-1 was operated with an open-ended membrane, while MABR-2 was initially operated with a closed end, but later was operated with periodic opening to vent lumen gases. De-oxygenated synthetic media (described below) was pumped through the flow cell. Each MABR had a recirculation pump and was connected to a purging reservoir, where the bulk liquid was sparged with N_2 to strip any residual DO from the reactor. Bulk liquid N_2 bubbles were vented in the reservoir before recycle line back to the flow-cell. This avoided any DO accumulation in the bulk liquid, which was a concern in the initial stages, prior to biofilm development. A magnetic stir bar kept the reservoir well-mixed with a high shear velocity, minimizing the attachment of biomass to the glass surface. An influent flow rate of 1 mL/min and a recirculation of 60 mL/min were provided to each MABR. Pure oxygen was supplied to the lumen of each at 0.05 atm relative pressure.

2.2. Synthetic medium for the MABRs

The synthetic wastewater for MABR-1 and MABR-2, was prepared from distilled water amended with 2.773 g Na_2HPO_4, 0.169 g KH_2PO_4, 0.410 g $MgSO_4{\cdot}7H_2O$ and 0.202 g$(NH_4)_2SO_4$ per liter, as well as a trace mineral and calcium iron solutions. Ca–Fe solution contained, per liter: 1 g $CaCl_2$-$2H_2O$ and 1 g$FeSO_4$-$7H_2O$. The trace mineral solution contained, per liter: 100 mg $ZnSO_4$ -$7H_2O$, 30 mg $MnCl_2$-H_2O, 300 mg H_3BO_3, 200 mg $CoCl_2$ -$6H_2O$, 10 mg $CuCl_2$ -$2H_2O$, 10 mg $NiCl_2$-$6H_2O$, 30 mg Na_2MoO_4-$2H_2O$, and 30 mg Na_2SeO_3. Potassium acetate was added as a COD source to achieve 30 mgCOD/L. The synthetic wastewater was maintained anoxic by sparging the medium with nitrogen gas and maintaining a positive pressure of nitrogen gas on the storage container. The pH was maintained at approximately 7, while the water temperature was 22 °C.

2.3. Analytical methods

Chemical oxygen demand (COD) was monitored in the influent and effluent of the MABR reactors using colorimetric methods (Hach, Loveland, CO, USA). A glass electrode pH meter was used to monitor pH.

For determining the biofilm thickness, we used a stereo-zoom light microscope (Cole-Palmer, Chicago, IL) equipped with a mounted digital camera (Cybershot DSC-F707, Sony) and a fiber-optic light source. The camera was fixed to the microscope with a 1 × mounting adapter. Biofilm thicknesses were measured using a microsensor by attaching it to a motorized micromanipulator with a vertical resolution of 0.010 mm. The microsensor tip was first positioned at membrane surface. Then, the tip was raised with the computer-controlled motor until the tip reached the outer edge of the biofilm, which was checked visually by microscopy. The distance was measured and recorded by SensorTrace Suit software (Unisense). Biofilm image acquisition was also performed in all seven flow-cell ports after four weeks of operation. Image processing for each measurement was followed by statistical evaluation of the results.

2.4. DO measurements

Clark-type oxygen microsensors (Unisense A/S, Denmark) with a 10 μm tip diameter were used to measure DO concentrations. The microelectrode movement was controlled with a micromanipulator (Model MM33-2, Unisense A/S). The use of microsensors is an invasive method that can slightly affect the results. However, considering that the tip was only 10 μm diameter and was immersed in a much thicker boundary layer, the microsensors would be expected to have a minimal impact on the DO concentration. Hydrodynamic measurements made by Hondzo et al. (2005), using a similar DO microsensor diameters and Reynolds number as used in this study, concluded that the disturbance of the flow by microsenors stem was minimal.

Longitudinal profiles of DO at the HFM surface were collected from the seven ports once the system reached steady state, typically after 2 h. For each port, transversal DO profiles were collected starting from the HFM surface, across the liquid diffusion layer (LDL), and into the bulk. The transversal DO measurements were collected at 20-μm intervals, typically reached a distance of around 1000 μm from the membrane surface. Profiles were collected at least in triplicate. For transient conditions, DO was measured continuously at the membrane surface, for one of the intermediate ports, during the shift from open-end to closed-end operation. Longitudinal steady-state DO profiles were also taken in both MABRs after four weeks of operation.

2.5. Calculation of membrane mass transfer coefficient, K_m

The membrane mass transfer coefficient, K_m, was calculated from oxygen transfer tests in clean membranes. We used measured transversal DO profiles in the diffusion-dominated liquid boundary layer, using the flux continuity condition. The oxygen flux across the HFM, $J_{O2,m}$, is equal to the diffusion flux through the mass transfer boundary layer at the membrane surface, $J_{O2,l}$, as follows:

$$J_{O2,m} = K_m\left(C_{O2,m(g)} - C_{O2,m(l)}\right) = D_{O2,l}\frac{dC_{O2,l}}{dr}\bigg|_{r=R_m} = J_{O2,l} \quad (1)$$

where $D_{O2,l}$ is the diffusion coefficient in the liquid phase (water), $C_{O2,l}$ is the measured oxygen concentration in water, $C_{O2,m}$ is the oxygen concentration in the microporous membrane on (g) gas side and (l) liquid side, and R_m the outer radius of the membrane. Given the small membrane thickness relative to the HFM radius, the membrane was approximated as a planar surface. From Eq. (1) the oxygen mass transfer coefficient in the membrane is calculated as:

$$K_m = \frac{D_{O2,l}(dC_{O2,l}/dr)_{r=Rm}}{C_{O2,m(g)} - C_{O2,m(l)}} \quad (2)$$

The oxygen diffusivity in water $D_{O2,l}$ was obtained from the literature (Haynes et al., 2015). The oxygen concentration in the gas side of the microporous membrane, $C_{O2,m(g)}$, is linked, by the ideal gas law, to the applied pressure and gas composition y_{O2} (either O_2 or air, at the working temperature). When determining the K_m, the HFM was operated in open end mode to minimize concentration changes. Also, microsensor measurements were carried out at the first port of the flow cell (from the left side), where the gas concentration was essentially equal to the supply concentration, $C_{O2,m(g)} = p\, y_{O2,in}/(RT)$. The oxygen gas concentration in the membrane, where it contacts the liquid, is related to the DO concentration in the liquid by the partition equilibrium (Henry's law), such that $C_{O2,m(l)} = (C_{O2,l})_{r=R_m}/H_{O2}$. Finally, microsensor measurements of concentration profiles of DO in water were used to determine the concentration gradient at the membrane surface, $(dC_{O2,l}/dr)_{r=Rm}$ and the concentration $(C_{O2,l})_{r=R_m}$. As mentioned above, profiles were collected at least in triplicate, and the reported K_m is the average of the replicates.

2.6. Numerical model for gas back-diffusion

A mathematical model for gas back-diffusion was developed, addressing both steady-state and transient conditions. The model included O_2 supply from the HFM lumen, and assumed that the bulk liquid was in equilibrium with 1 atm of N_2. The model was implemented with the finite-element simulation platform COMSOL Multiphysics (COMSOL 4.4, Comsol Inc., Burlington, MA, www.comsol.com).

The numerical model included fluid flow and mass transport of O_2 and N_2, both in the liquid surrounding the HFM and in the lumen gas (Fig. 3). For the flow and mass transport in the liquid phase, a two-dimensional (2-D) axisymmetric geometry was set along the axis of the membrane lumen (direction x) with radial gradients along direction r. The 2-D model implies an annular cross-section for the flow, with size $L_f = 3.4$ mm (the radius of a circle with the same area as the square cross-section). This model was coupled with a one-dimensional (1-D) domain for gas flow and mass transport in the membrane lumen (assuming no radial gradients in the lumen).

2.6.1. Flow and mass transport in the liquid

The liquid velocity distribution in the flow cell was determined by solution of the two-dimensional Navier-Stokes Eqs. (3) and (4) in the 2-D axisymmetric domain:

$$\rho(\mathbf{u}_l \cdot \nabla)\mathbf{u}_l = \nabla \cdot \left[-p\mathbf{I} + \mu\left(\nabla\mathbf{u}_l + (\nabla\mathbf{u}_l)^T\right)\right], \quad (3)$$

$$\nabla \cdot \mathbf{u}_l = 0 \quad (4)$$

where $\mathbf{u}_l$ is the water flow velocity, p is the pressure, ρ is the water density, μ is the liquid dynamic viscosity, and $\mathbf{I}$ is the identity matrix. The water velocity was assumed to be zero at the membrane surface and at the flow cell wall (non-slip condition, $\mathbf{u}_l = 0$). Laminar flow conditions were imposed, with average velocity u_{in} in the inlet and zero relative pressure in the outlet.

The mass transport of oxygen and nitrogen in the liquid flow results from convection-diffusion Eqs. (5) and (6) solved for the dissolved O_2 and N_2 concentrations, $C_{O2,l}$ and $C_{N2,l}$:

$$\mathbf{u}_l \nabla C_{O2,l} = D_{O2,l}\nabla^2 C_{O2,l}, \quad (5)$$

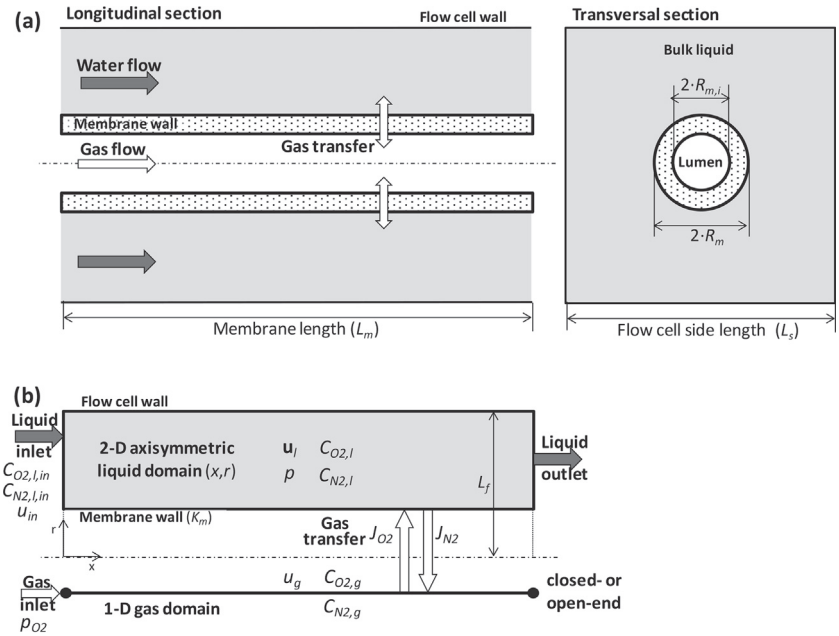

Fig. 3. (a) Schematic representation (not at scale) of the experimental co-current aeration system with a single HFM inside a square-section flow cell filled with liquid. Water flows between the HFM and the flow cell wall, and the membrane is supplied with oxygen. (b) Model representation including a 2-D axisymmetric liquid domain connected via the membrane wall with a 1-D gas domain.

$$\mathbf{u}_l \nabla C_{N2,l} = D_{N2,l} \nabla^2 C_{N2,l} \quad (6)$$

where $D_{O2,l}$ and $D_{N2,l}$ are the diffusion coefficients in the liquid. Constant dissolved O_2 and N_2 concentrations were imposed at the inlet boundary, $C_{O2,l,in}$ and $C_{N2,l,in}$. N_2 was present in the feed water at 18 mg/L, which corresponds to equilibrium with 1 atm of N_2. Convection-only outlet boundary was assigned ($\partial C_{O2,l}/\partial x = \partial C_{N2,l}/\partial x = 0$), while no-flux conditions were imposed at the flow cell wall ($\partial C_{O2,l}/\partial y = \partial C_{N2,l}/\partial y = 0$). On the membrane wall, flux continuity conditions were set:

$$J_{O2} = K_m (C_{O2,g} H_{O2} - C_{O2,l}), \quad J_{N2} = K_m (C_{N2,g} H_{N2} - C_{N2,l})$$

where H_{O2} and H_{N2} are the gas-liquid partition (Henry's) coefficients at 20 °C. We assumed that the membrane, which was microporous, had the same selectivity for O_2 and N_2 (Ahmed and Semmens, 1992a), which translates to the same K_m.

2.6.2. Flow and mass transport in the gas

The mass balances for the gases in the membrane lumen were adapted from Ahmed and Semmens (1992a), who modeled steady-state O_2 and N_2 profiles in a closed-end HFM. Unlike the past model, our model includes transient behavior, and used computational fluid dynamics to determine dissolved gas concentrations in the fluid along the membrane length. Frictional gas pressure losses in the lumen were included, and the model allowed for transient conditions to be simulated, for example when switching from open-end to closed-end operation. Finally, the membrane mass transfer resistance (K_m) was considered explicitly. Note that only longitudinal gradients in gas concentrations (direction x) were considered in our model.

In both closed-end and open-end operation, the one-dimensional transient mass balances for O_2 (Eq. (7)) and N_2 gas (Eq. (8)) in the membrane lumen included transport by convection and diffusion, and transfer across the wall into or from the liquid phase. These equations allowed the concentrations $C_{O2,g}(t, x)$ and $C_{N2,g}(t, x)$ to be calculated.

$$\frac{\partial C_{O2,g}}{\partial t} = \frac{\partial}{\partial x}\left(D_g \frac{\partial C_{O2,g}}{\partial x} - u_g C_{O2,g}\right) - \frac{2}{R_m} K_m (C_{O2,g} H_{O2} - C_{O2,l}) \quad (7)$$

$$\frac{\partial C_{N2,g}}{\partial t} = \frac{\partial}{\partial x}\left(D_g \frac{\partial C_{N2,g}}{\partial x} - u_g C_{N2,g}\right) - \frac{2}{R_m} K_m (C_{N2,g} H_{N2} - C_{N2,l}) \quad (8)$$

In Eqs. (7) and (8), u_g is the gas velocity in the fiber, while $C_{O2,l}$ and $C_{N2,l}$ are the corresponding dissolved O_2 and N_2 concentrations, respectively, at position x. The same mass transfer coefficient through the membrane, K_m, and the same diffusion coefficient in the gas phase, D_g, was assumed for both gases.

The gas velocity in the lumen was calculated differently for close-end or open-end operation. In the closed-end operation, frictional losses were neglected due to the very low gas velocity in the lumen. For this case, the sum of gas concentrations at any point x is equal to that of the inlet: $C_{O2,g} + C_{N2,g} = C_{O2,in} + C_{N2,in} =$ constant. In these conditions, the sum of Eqs. (7) and (8) is equal to zero. Adding Eqs. (7) and (8), and rearranging, results in:

$$\frac{du_g}{dx} = -\frac{2K_m (C_{O2,g} H_{O2} - C_{O2,l} + C_{N2,g} H_{N2} - C_{N2,l})}{R_m (C_{O2,in} + C_{N2,in})} \quad (9)$$

which allows for calculation of the local gas velocity along the fiber, $u_g(x)$, resulting from the diffusion of gasses into or out of the membrane. At the sealed end, the gas velocity must be zero ($u_g = 0$ at $x = L_m$). The inlet concentrations were calculated from the universal gas law, for example, $C_{O2,g,in} = p\, y_{O2,in}/(RT)$ with $y_{O2,in}$ the oxygen fraction in the inlet gas (i.e., 1 for pure oxygen or 0.21 for air). In model simulations for the parametric study, only pure oxygen was used, i.e., $C_{N2,g,in} = 0$.

For the open-end HFM, the constant gas velocity u_g was calculated from the Hagen-Poiseuille relationship, which is valid for slightly compressible fluids (Federspiel et al., 1996):

$$u_g = \frac{R_{m,i}^2}{8\mu_g L_m}(p_{in} - p_{out})$$

where μ_g is the gas dynamic viscosity and $R_{m,i}$ is the internal fiber radius. The inlet pressure p_{in} was defined according to the measured value, while the outlet pressure p_{out} was set as atmospheric pressure.

The boundary conditions for Eqs. (7) and (8) imply constant concentrations in the inlet $C_{O2,g,in}$ and $C_{N2,g,in}$ at $x = 0$. At $x = L_m$,

Table 1
Model parameters.

Parameter	Symbol	Value	Units	Reference
Physical parameters				
Water density	ρ	1000	kg/m^3	(Haynes et al., 2015)
Water dynamic viscosity	μ	0.001	Pa·s	(Haynes et al., 2015)
Gas dynamic viscosity	μ_g	$1.8 \cdot 10^{-5}$	Pa·s	(Haynes et al., 2015)
O_2 diffusion coefficient in water	$D_{O2,l}$	$2 \cdot 10^{-9}$	m^2/s	(Haynes et al., 2015)
N_2 diffusion coefficient in water	$D_{N2,l}$	$1.7 \cdot 10^{-9}$	m^2/s	(Haynes et al., 2015)
O_2 and N_2 diffusivity in gas	D_g	$1.76 \cdot 10^{-5}$	m^2/s	(Haynes et al., 2015)
Henry coefficient for O_2	H_{O2}	0.0338	mol(aq.)/mol(g)	(Haynes et al., 2015)
Henry coefficient for N_2	H_{N2}	0.0156	mol(aq.)/mol(g)	(Haynes et al., 2015)
Ideal gas constant	R	$8.206 \cdot 10^{-5}$	m^3·atm/(mol·K)	–
Membrane parameters				
Mass transfer coefficient	K_m	$5.4 \cdot 10^{-5}$	m/s	Fitted to experiments
Length	L_m	0.32	m	Experimental
		2.5	m	Parametric study
Outer radius	R_m	140	μm	Mitsubishi Rayon
Inner radius	$R_{m,i}$	130	μm	Mitsubishi Rayon
Operation conditions				
Oxygen inlet liquid concentration	$C_{O2,l,in}$	0	mol/m^3	Experimental
Nitrogen inlet liquid concentration	$C_{N2,l,in}$	0.64	mol/m^3	Experimental
Oxygen inlet gas concentration	$C_{O2,g,in}$	69.7	mol/m^3	Experimental
Nitrogen inlet gaseous concentration	$C_{N2,g,in}$	0	mol/m^3	Experimental
Inlet gas pressure	p_{in}	1.07 and 1.18	atm	Experimental
		1.68	atm	Parametric study
Outlet gas pressure (for open-end)	p_{out}	1	atm	Experimental
Average liquid velocity	u_{in}	1 and 5	mm/s	Experimental
Venting interval	t_c	1, 2, 5, 10 and 30	min	Parametric study
Venting open-end duration	t_o	20	s	Parametric study
Temperature	T	293.15	K	Experimental

zero diffusion was assumed for the open-end case, while for the closed-end zero total flux was imposed, which in both cases leads to:

$$\frac{\partial C_{O2,g}}{\partial x}(t, x = L_m) = 0, \quad \frac{\partial C_{N2,g}}{\partial x}(t, x = L_m) = 0$$

Initial gas concentrations for the entire membrane were equal to the inlet concentrations.

Predicted DO concentrations at the surface of the fiber ($C_{O2,l}$) were directly compared with experimental measurements for both steady and transient states. Several model parameters were taken from the experimental conditions, such as membrane thickness, average water velocity, membrane length and radius, dissolved nitrogen, dissolved oxygen in the influent water, and oxygen gas pressures in the membrane inlet and outlet. For the model application, parametric studies were used, where simulations were carried out for a range of values of a single parameter. These and other parameters obtained from literature are summarized in Table 1.

3. Results and discussion

3.1. Determination of membrane mass transfer coefficient

A typical plot of measured DO profiles, perpendicular to the membrane surface, is shown in Fig. 4. From the slope of the measured DO concentration profile, the flux of oxygen was calculated with Eq. (1). Subsequently, the mass transfer coefficient K_m was calculated from Eq. (2). An average K_m value of 5.4×10^{-5} m/s was obtained. This value is consistent with previously determined oxygen mass transfer coefficients for the same membrane (Ahmed et al., 2004) who found $K_m = 5 \times 10^{-5}$ m/s. In this study, the mass transfer coefficients for N_2 and O_2 were assumed to be equal.

3.2. Model evaluation

The back-diffusion model results were in good agreement with the measured values of DO along the membrane length, both for open- and closed-end operation, in steady state and transient conditions (Fig. 5).

For closed ends using either air or pure O_2 supplied in co-current with the liquid flow (u_{in} = 5 mm/s), the N_2 back-diffusion significantly reduced the DO concentrations along the membrane length. The DO concentrations decreased from 35 mg/L to 5 mg/L when pure O_2 was supplied, and from 6 mg/L to 0.5 mg/L in case of air (Fig. 5a). Accordingly, the steady state partial pressure of O_2 in the membrane lumen significantly decreased as O_2 was replaced by N_2 (Fig. 5b). However, for the open-end operation, O_2 concentrations remained almost constant and at high values until the distal end of the membrane (Fig. 5a). The open-end operation mode typically resulted in negligible back-diffusion effects. The partial pressure of O_2 in the gas decreased only slightly along the membrane because of the frictional pressure loss (Fig. 5b).

The counter-current configuration showed lower DO concentrations towards the end of the membrane than the co-current configuration, in stationary conditions at an average water velocity of u_{in} = 1 mm/s (Fig. 5c). When water flows in the opposite direction of the supplied gas, i.e., in counter-current operation, O_2 transferred to the bulk liquid from the membrane does not accumulate downstream of the flow cell, thus decreasing DO concentrations in the liquid towards the closed end of the membrane. Therefore, the rest of the simulations considered only co-current operation. The partial pressure of O_2 in the counter-current operation decreases more than in the co-current because of the larger driving force for the trans-membrane transfer at the distal end, which is created by the oxygen-free influent water.

The model also accurately predicted the transient behavior of the DO concentration after suddenly closing the distal end of the membrane. The DO profile began with the steady state value in open-end operation, and progressively decreased towards the steady state value for the closed-end period. The experimental values and model predictions for the Port 4 are shown in Fig. 5e. The time required to reach a steady O_2 profile in the lumen during the back-diffusion process was around 30 min.

3.3. Model-based assessment of periodic venting

Closed-end HFMs initially have high gas transfer rates, as the membranes are filled with pure O_2. However, the rates quickly decrease as gas back-diffusion profiles develop. We used numerical modeling to study the effects of periodically venting closed-end membranes, temporarily returning the membranes to the initial condition by venting the back-diffusion gases. The transitory gas dynamics of periodic venting were studied, and the impacts of

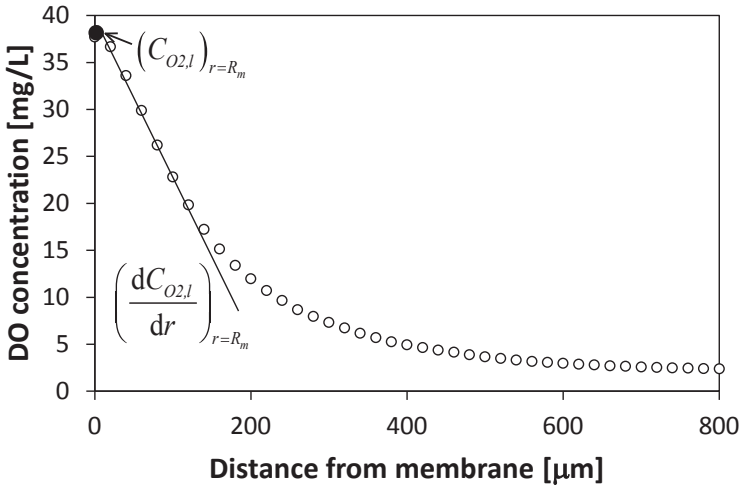

Fig. 4. A representative profile of measured dissolved oxygen concentration through the mass transfer boundary layer in the liquid adjacent to the membrane. From this profile, the concentration and the normal gradient of concentration at the membrane surface ($d = 0$ from membrane, which means $r = R_m$ in the numerical model) were extracted to calculate K_m.

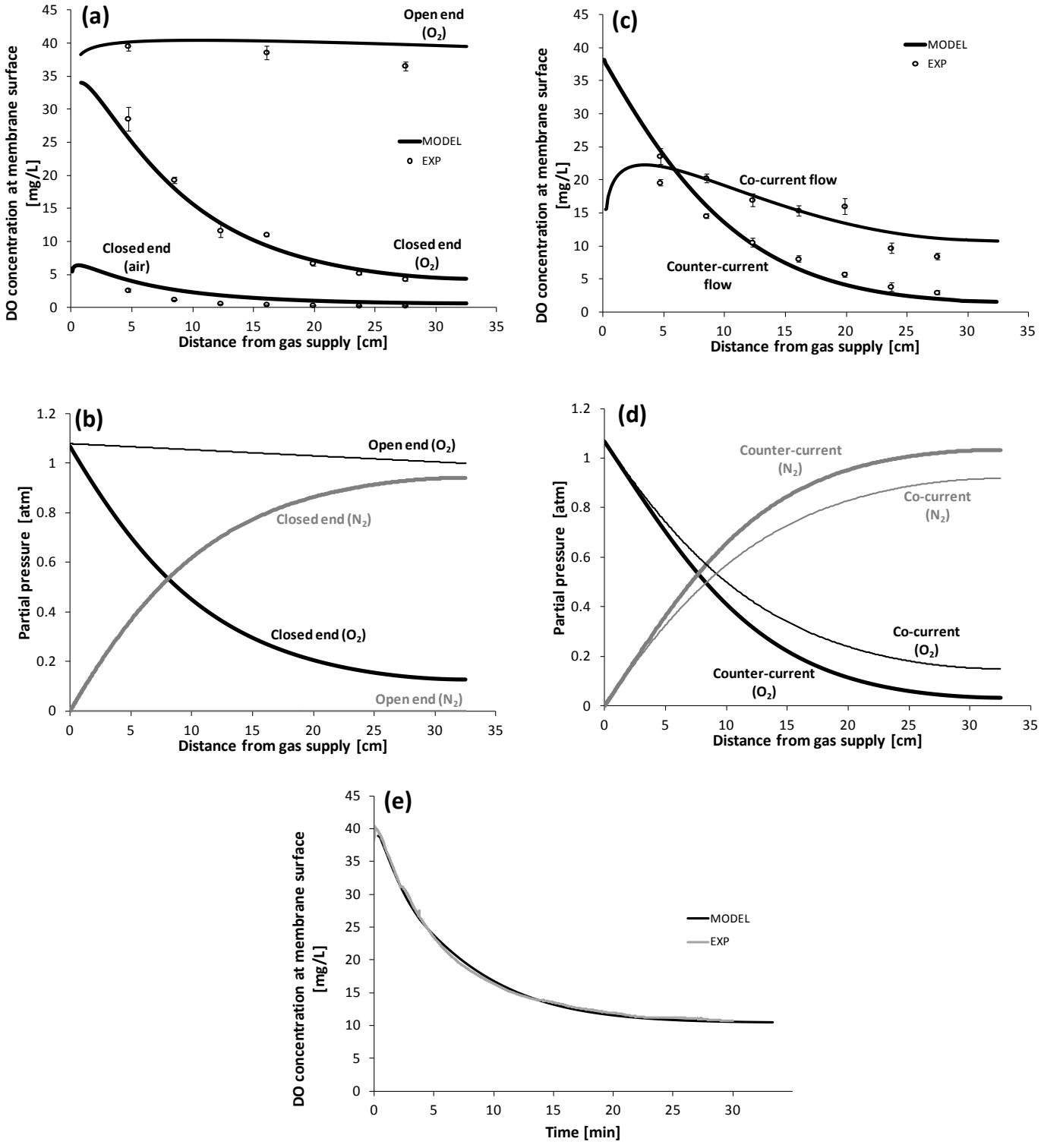

Fig. 5. Experimental and model-simulated dissolved oxygen (DO) profiles at the membrane surface for the experimental HFM flow cell. Liquid and gas flows are co-current, unless indicated otherwise. (a) DO profiles for open and closed end operation modes using an inlet relative gas pressure of 0.18 atm and $u_{in} = 5$ mm/s. DO profiles for air and oxygen as supply gases are shown for the closed end cases; (b) Simulations of partial pressures for O_2 and N_2 in the open-end and closed-end with pure O_2 supply; (c) DO profiles along the membrane length for closed-end mode in co- and counter-current flow configurations using pure oxygen at 0.07 atm and $u_{in} = 1$ mm/s; (d) Simulations of partial pressures for O_2 and N_2 in the closed-end co- and counter-current operation with pure O_2 supply; (e) DO concentrations over time when transitioning from an open-end to a closed-end operation using pure O_2 at an inlet pressure of 0.18 atm. The microsensor measurement was performed at the membrane surface, for Port 4 at 16.1 cm from the inlet. Error bars in plots (a) and (c) are the standard deviation of triplicate measurements.

different membrane opening intervals on OTRs and OTEs were explored.

Time-averaged O_2 partial pressures during three venting cycles were calculated from simulations with $R_m = 140$ μm, $K_m = 5 \times 10^{-5}$ m/s, a longer membrane ($L_m = 2.5$ m) than in the experimental setup (closer to what might be used in a full-scale MABR) and an inlet gas pressure of $p_{in} = 1.68$ atm. Each cycle included a 30-min closed period followed by a 20-s open (venting) period. This corresponds to a 30-min "venting interval". Fig. 6 shows how, during the first cycle from $t = 0$ to $t = 30$ min (closed phase), a drop in the membrane-averaged O_2 partial pressure developed due to back-diffusion. Before the steady-state back-diffusion condition was fully obtained, the membrane was opened for 20 s, allowing the O_2 partial pressures along the membrane to recover their maximum value, which was slightly lower (1.54 atm) than the inlet gas pressure due to the pressure drop resulting from high gas velocities in open-end periods. The Hagen-Poiseuille relationship for slightly compressible fluids effectively predicted the observed flows for a broad range of pressures, ranging from 0.07 to 0.68 atm (data not shown).

This periodic venting provides high OTEs during most of the cycle duration, while maintaining higher time-averaged O_2 partial pressures than closed-end membranes. These results indicate that a 20-s open phase every 30 min was sufficient to allow oxygen pressure to recover its maximum value (1.54 atm) before the next closed phase. On the other hand, the membrane-averaged oxygen partial pressure dropped from 1.54 to 0.86 atm during the closed-end phase. On average, the membrane had a higher O_2 pressure than in the steady-state, closed-end operation. Therefore, it provided a greater OTR than the purely closed-end mode.

To evaluate how the duration of the closed-end/open-end cycles influenced the OTRs and OTEs, we simulated different venting intervals (i.e., time between openings) ranging from 1 to 30 min, with a constant venting (open end) duration of 20 s (Fig. 7). The predicted average OTRs were 2–4 times higher than with permanently closed end. Furthermore, the OTE values (75–99%) were comparable to the closed end (100%), and dramatically higher than the open end mode (0.5%).

Interestingly, when the venting interval decreased below approximately 20 min, the OTR values were higher than for purely open-end operation, without significantly affecting the OTEs. This can be explained by the simulated O_2 pressure profiles along an HFM for open-end steady-state conditions, closed-end steady state conditions, and for the transition from open-end to closed-ended conditions (Fig. 8). Profiles for the transition phase are presented at different times. For open-end operation, the O_2 pressure decrease is mainly due to frictional losses, whereas in closed-end operation the O_2 pressure drop is caused by back-diffusion. Furthermore, for the closed-end case, the O_2 concentration decreases from a constant initial value (equal to the inlet pressure of 1.68 atm), along the whole membrane until the steady state profile is reached. The shape of the transient profiles shows that, initially, N_2 back-diffusion only affects the initial portion of the HFM. This is where pure O_2 is supplied, and also where O_2-free water enters the system, providing the maximum O_2 and N_2 concentration gradients. Then the N_2/O_2 gas mixture is transferred by advective flow towards the distal end of the membrane.

The time-dependent reduction in the O_2 pressure profiles occurs during the closed phase of a venting cycle. If the venting interval is smaller, the time- and length-averaged O_2 pressure concentrations increase, leading to higher OTRs. However, below a certain venting interval, the OTRs actually exceed those of the open-end configuration. This is caused by the pressure drop resulting from high gas velocities in open-end configuration. However, the pressure losses are negligible once the membrane is closed, thus allowing a higher total average pressure inside the membrane (see pressure profiles at times t_0, t_1, and t_2 in Fig. 8).

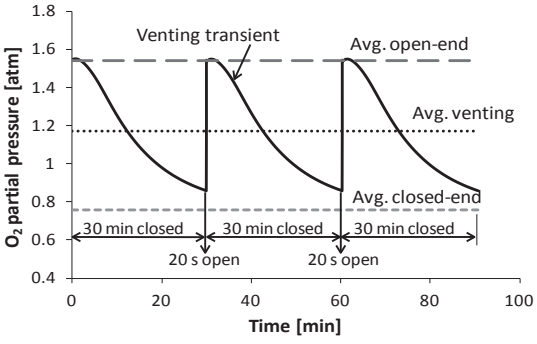

Fig. 6. Simulated O_2 partial pressures in the lumen, averaged along the entire membrane length for different operation regimes: (i) transient (solid line) and time-averaged (dotted line) during three venting cycles, (ii) steady state closed end (short-dashed gray line), and (iii) steady state open end (long-dashed gray line).

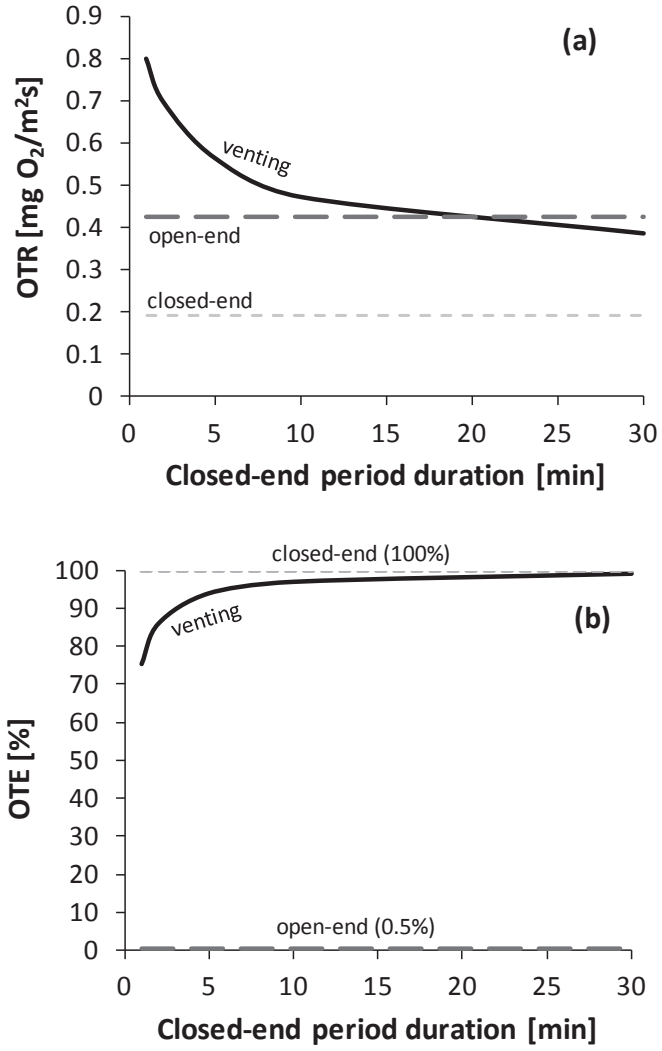

Fig. 7. Comparison of simulated (a) oxygen transfer rates (OTR) and (b) oxyge transfer efficiencies (OTE) for open operation, closed operation, and intermittent opening. Venting mode was tested for venting intervals (time between ventings) ranging from 1 to 30 min, with 20 s open phases.

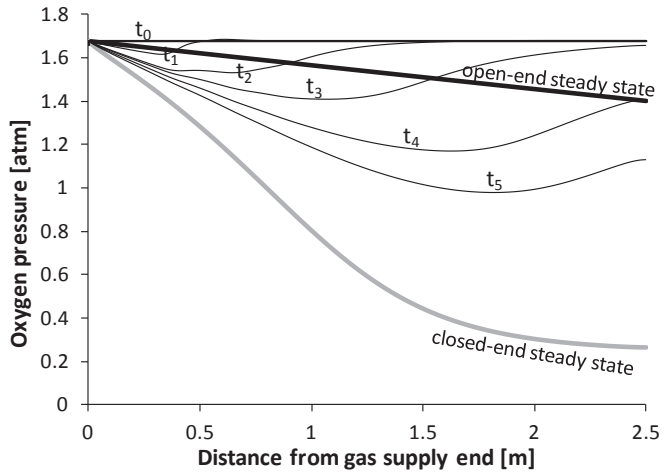

Fig. 8. Oxygen partial pressure profiles along the membrane length for open-end (thick black line) and closed-end (thick gray line) steady state conditions, and time-averaged for transient conditions from open- to closed-end (thin black lines). The transient pressures are averages in time between the initial time and $t_1 = 2$ min, $t_2 = 5$ min, $t_3 = 10$ min, $t_4 = 20$ min, and $t_5 = 30$ min. Steady state conditions were essentially achieved after 60 min.

The model results clearly indicate that periodic venting of closed-end operation can improve the gas transfer rates beyond those obtainable with conventional open-end operation, while maintaining high mass transfer efficiencies.

A simple calculation was made to compare different gas supply modes and show how the venting strategy could impact the MABR design, such as membrane area and required oxygen supply. Table 2 shows the OTRs, OTEs, required membrane areas, and O_2 supply needs using simulation results for the conditions in Fig. 7. The membrane area was calculated for an arbitrary O_2 requirement. Oxygen supply requirements were determined by multiplying the OTE by the O_2 need. Finally, membrane areas and O_2 supply requirements for open-end and venting modes were normalized to the values for closed-end operation (first row in Table 2). Calculations indicate that the open-end operation requires only half of the membrane area of the closed-end operation. However, around 200 times more O_2 is required. With the intermittent venting of 20 s every 30 min, the required membrane area is the same as the open end, i.e., half of the area required for the closed-end operation. But O_2 requirement is essentially the same as the closed-end operation.

3.4. Experimental assessment of gas supply strategies on HFMs with biofilm

The periodic venting strategy was tested in a bench-scale MABR treating COD. Fig. 9 shows the biofilm thicknesses and measured DO concentration profiles along the membrane surface in two MABRs that were run in parallel. MABR-1 was operated in open-end mode, and MABR-2 was operated in closed-end mode. Biofilm thickness images and measurements of DO profiles were taken after four weeks of operation.

In MABR-1 (open end), a homogeneous biofilm grew through the fiber surface, with a similar thickness along the membrane length (Fig. 9a). In MABR-2 (closed end), the biofilm was thick at the gas supply end, but was significantly reduced towards the sealed end of the membrane (Fig. 9 b). This can be explained by the measured DO profiles along the membrane (Fig. 9 c and d). For MABR-1, the O_2 concentrations remained almost constant and at high values across the entire membrane (Fig. 9 c). This is because the high supply gas rate into the membrane resulted in negligible back-diffusion effects. The partial pressure of O_2 in the gas decreased only slightly along the membrane because of frictional pressure loss. N_2 accumulation in the membrane was not significant in MABR-1, as inlet gas flow-rate was high enough to vent back-diffused N_2 to the atmosphere. However, for MABR-2, O_2 consumption and N_2 back-diffusion significantly reduced O_2 concentrations along the fiber length (Fig. 9 d) resulting in much lower OTRs and consequently lower overall COD removal fluxes (Fig. 10).

The open-end MABR-1 had a higher average O_2 pressure than in the steady-state, closed-end MABR-2 (Fig. 9 c and d). Therefore, it provided a greater OTRs and COD removal fluxes than the purely closed-end MABR-2 (Fig. 10). The average COD removal flux for MABR-1 was double the value for MABR-2. In MABR-2, back-diffusion caused DO limitation in much of the membrane. This slowed the development of the biofilm, and consequently the increase in COD removal. Also, COD removal rates fluctuated considerably because this was a small reactor. As the biofilms grew, any biofilm detachment had a significant impact on the system. This would be more likely to average out in a larger system.

Note that the predicted OTR values for closed, open and venting strategies in a clean membrane were lower than those for MABRs. This is because the biofilm can eliminate the mass transfer resistance of the liquid concentration boundary layer (Semmens, 2008).

After four weeks of operation, MABR-2 was switched to periodic venting, which consisted of opening the membrane (venting) for 20 s every 20 min. Fig. 10 shows the experimental COD removal fluxes that were obtained when periodic venting cycles were applied to MABR-2. Fig. 11 shows the biofilm thicknesses along the membrane length prior to venting, and after eight days of venting cycles.

The mathematical model predicted that greater average O_2 partial pressures, and consequently higher OTRs and removal fluxes, could be obtained by applying periodic venting to a closed-end MABR. The experimental COD removal fluxes are shown in Fig. 10. The average COD removal flux became double that for the closed-end operation, increasing from 56 gCOD/m^2d to 117 gCOD/m^2d. This value is very similar to the 121 gCOD/m^2d obtained in MABR-1 (Fig. 10). This was in part due to the more uniform biofilm thickness along the length of the fiber when periodic venting was implemented (Fig. 11). Based on the measured gas flow rate through the membrane during the open cycles, OTEs of at least 97% were obtained when applying the periodic venting. In this research, the COD removal rates were greater than those obtained in some previous MABR studies. This was mainly because we used pure oxygen as the supplied gas. Also, we used acetate as organic carbon source. Acetate is readily biodegradable substrate, as opposed to more complex organics such as wastewater. Nevertheless, COD removal rates found in this study were similar than the ones obtained by Osa et al. (1997), Pankhania et al. (1999) and Brindle et al.

Table 2
Required membrane areas and oxygen fluxes for closed-end, open-end, and venting modes. Areas and fluxes are normalized by the closed-end value.

Case	OTR (mg $m^{-2}s^{-1}$)	OTE (%)	Normalized required membrane area	Normalized O_2 supply requirement
Closed end	0.19	100	1.0	1.0
Open end	0.42	0.47	0.5	213
Venting ($t_c = 1$ min, $t_o = 20$ s)	0.79	75.3	0.2	1.3
Venting ($t_c = 30$ min, $t_o = 20$ s)	0.38	98.9	0.5	1.0

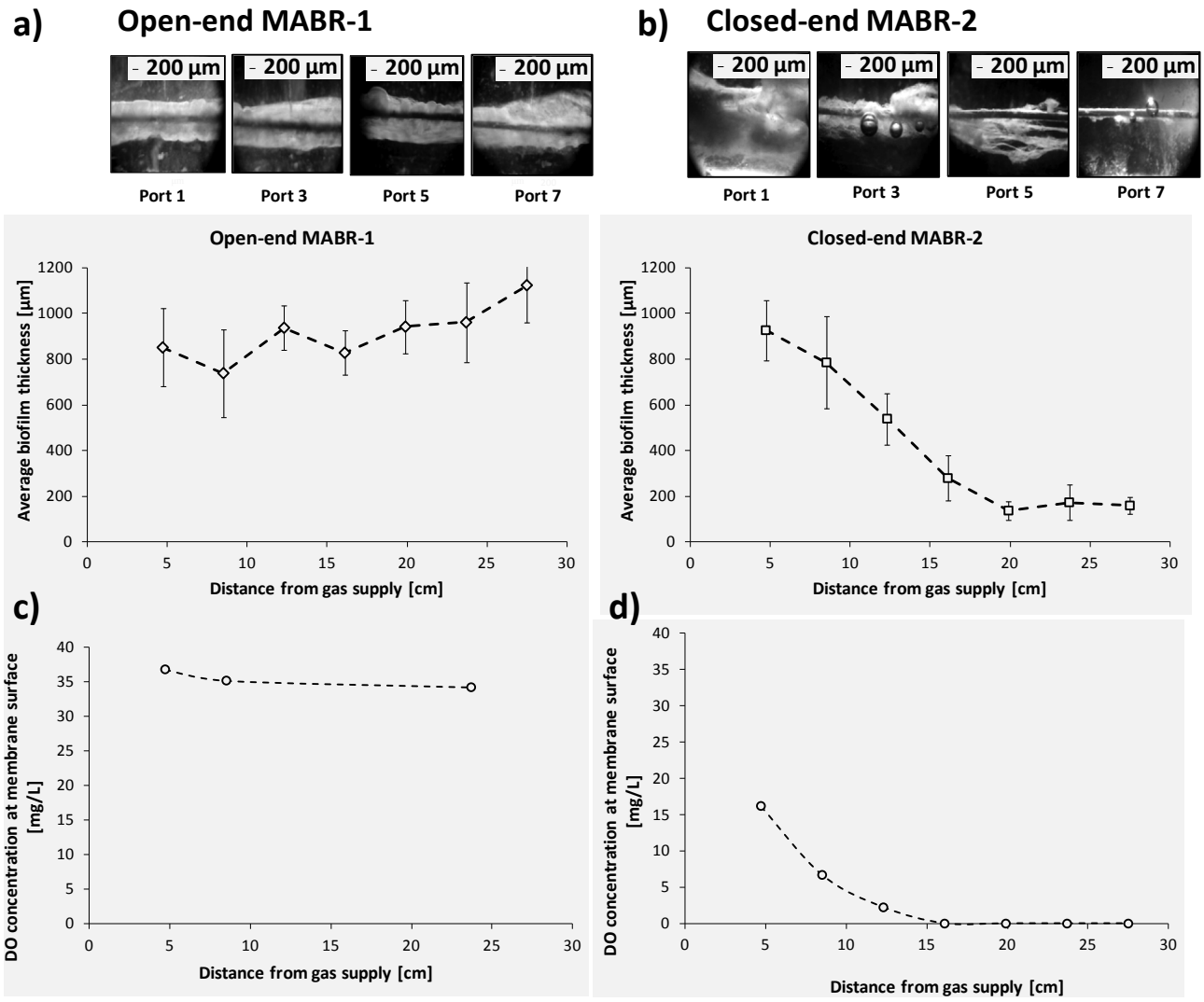

Fig. 9. Biofilm thickness development along the membrane length in normally operated open-end MABR-1 (a) and closed-end MABR-2 (b). Experimental DO profiles at membrane surface for open-end MABR-1 (c) and closed-end MABR-2 (d). Port 1 is 4.7-cm from gas supply (left side), and Ports 3, 5, and 7 are at 7.6-cm increments from Port 1.

(1999), who reported COD removal rate values in MABRs fed with pure O_2 of 180, 42.7, 62.6 gCOD/m^2d respectively. Experimental results verified that periodic venting of closed-end MABRs can lead to high OTRs and OTEs, improving the overall process performance and increasing the energy efficiency.

This work highlights the potential transient behavior of gas back-diffusion, and the potentially significant lag in reaching steady state operation after a perturbation. For example, changing the supply gas pressure, concentration of supply gas in the liquid phase, and concentration of back-diffusion gases in the liquid phase, among others. Following any of these changes, it may take a considerable amount of time to reach steady state.

The optimal venting interval (time between openings) and venting time (open period) depends on a variety of factors, including the membrane mass transfer coefficient, diameter, length, supply gas pressure and concentration, and dissolved gas concentrations in the liquid. For instance, larger membrane diameters will likely allow a greater venting interval, as there is greater gas storage in the membrane lumen relative to the gas transfer across the membrane. Larger HFM diameters, and longer membrane lengths, would require longer venting periods. When selective membranes are used, the relationship between the diffusion coefficients can also be important. Finally, the effect of liquid flow in a contactor, e.g., co-current, counter-current, or cross flow, can impact the gas transfer rates and the transition to steady-state conditions. Future research should explore the impact of the above factors in more detail.

Past research on MABRs has shown that water vapor can diffuse into the membrane and condense at the sealed end, plugging part of the membrane (Côte et al., 1988, 1989., Fang et al., 2004). However, it would take weeks or months for condensation to have an appreciable effect on the membrane behavior. In our closed-end experiments, the membranes were vented every two days, and no sign of condensate accumulation was observed during the ventings. Some MABRs are periodically vented to remove water condensation, but the frequency of venting is typically too low to obtain the gas transfer rate benefits. Based on our findings, it would be easy to increase the venting frequency to both remove condensate and obtain higher OTRs.

The above strategy was studied for O_2 supply to an MABR, but the periodic venting is also relevant to MABRs supplied with air, or MBfR applications with gases such as hydrogen gas (H_2) or methane (CH_4) (Martin and Nerenberg, 2012; Shi et al., 2013).

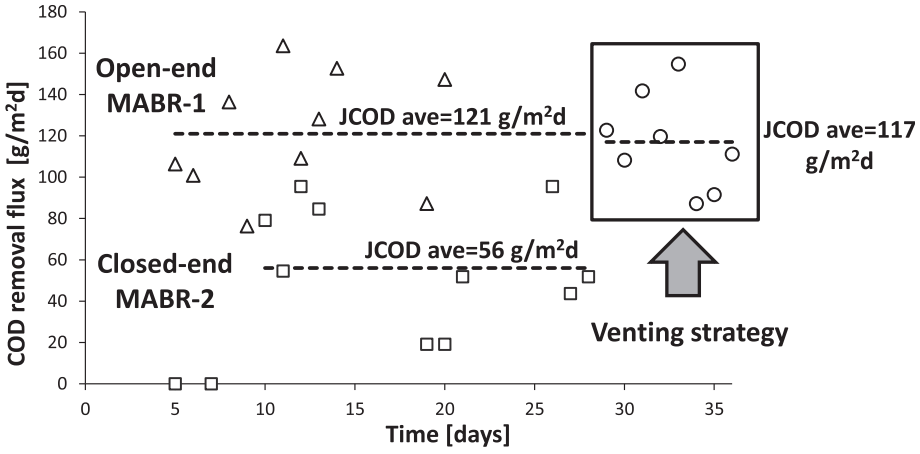

Fig. 10. Experimentally observed COD removal fluxes in MABR-1 (triangles) and MABR-2 (squares) plotted against time. Circles enclosed in the black rectangle represent COD removal fluxes for the closed-end MABR-2 when a venting strategy of 20 s open and 20 min closed was implemented.

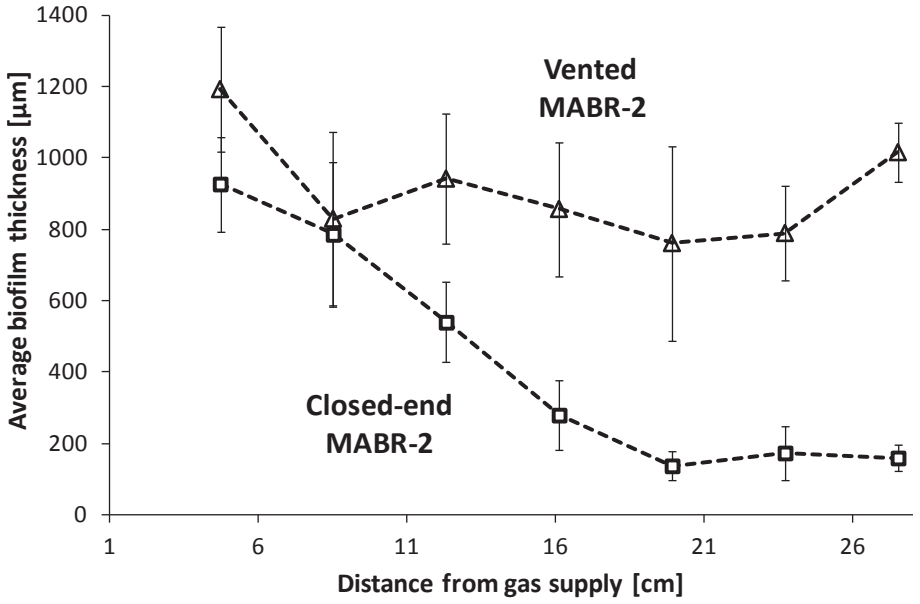

Fig. 11. Biofilm thicknesses along the fiber length of MABR-2 just prior to initiating the venting cycles, and after eight days of periodic venting. Venting provides a much more uniform biofilm thickness.

4. Conclusions

The periodic venting of lumen gases in a closed-end MABR can greatly improve the membrane's OTRs and contaminant removal fluxes, without significantly impacting the OTEs. This is due to the transient behavior of the lumen gas profiles when shifting from open-end to closed-end operation. When the venting interval is short enough, the OTR can be even higher than with continuous open-end operation. This novel gas supply strategy can greatly increase the capacity of MABRs, and decrease the capital and operating cost of new systems. Future research should address in more detail the range of factors that affect the selection of opening interval, the closed duration, and the impacts of these factors on the OTRs and OTEs.

Acknowledgements

Primary funding for this work was from Water Environment Research Foundation (WERF) project U2R14. Additional funding was provided by the Basque Government, partially financing Patricia Pérez through a fellowship, and the joint Spanish Ministry of Economics and Competitiveness and European Regional Development Fund (FEDER) project “Innovative Integrated Biological Processes for Nutrients Removal (PBi2)” (CTM2012-36227).

References

Ahmed, T., Semmens, M.J., 1992a. The use of independently sealed microporous hollow fiber membranes for oxygenation of water - model development. J. Membr. Sci. 69 (1–2), 11–20.
Ahmed, T., Semmens, M.J., 1992b. Use of sealed end hollow fibers for bubbleless membrane aeration - experimental studies. J. Membr. Sci. 69 (1–2), 1–10.
Ahmed, T., Semmens, M.J., Voss, M.A., 2004. Oxygen transfer characteristics of hollow-fiber, composite membranes. Adv. Environ. Res. 8, 637–646.
Aybar, M., Pizarro, G., Boltz, J.P., Downing, L., Nerenberg, R., 2014. Energy-efficient wastewater treatment via the air-based, hybrid membrane biofilm reactor (hybrid MfBR). Water Sci. Technol. 69 (8), 1735–1741.
Brindle, K., Stephenson, T., Semmens, M.J., 1998. Nitrification and oxygen utilisation in a membrane aeration bioreactor. J. Membr. Sci. 144, 197–209.
Brindle, K., Stephenson, T., Semmens, M.J., 1999. Pilot-plant treatment of a high-strength brewery wastewater using a membraneaeration bioreactor. Water

Environ. Res. 71 (6), 1197–1204.
Castagna, L., Zanella, A., Scaravilli, V., Magni, F., Deab, S.A.E., Introna, M., Mojoli, F., Grasselli, G., Pesenti, A., Patroniti, N., 2015. Effects on membrane lung gas exchange of an intermittent high gas flow recruitment maneuver: preliminary data in veno-venous ECMO patients. J. Artif. Organs 18 (3), 213–219.
Côte, P., Bersillon, J.L., Huyard, A., 1989. Bubble-free aeration using membranes - mass-transfer analysis. J. Membr. Sci. 47 (1–2), 91–106.
Côte, P., Bersillon, J.L., Huyard, A., Faup, G., 1988. Bubble-free aeration using membranes - process analysis. J. Water Pollut. Control Fed. 60 (11), 1986–1992.
Downing, L.S., Nerenberg, R., 2008. Total nitrogen removal in a hybrid, membrane-aerated activated sludge process. Water Res. 42 (14), 3697–3708.
Fang, Y., Clapp, L.W., Hozalski, R.M., Novak, P.J., Semmens, M.J., 2004. Membrane gas transfer under conditions of creeping flow: modeling gas composition effects. Water Res. 38 (10), 2489–2498.
Federspiel, W.J., Henchir, K.A., 2004. Encyclopedia of Biomaterials and Biomedical Engineering. Marcel Dekker, Inc., Pittsburgh, PA.
Federspiel, W.J., Williams, J.L., Hattler, B.G., 1996. Gas flow dynamics in hollow-fiber membranes. Aiche J. 42 (7), 2094–2099.
Haynes, W.M., Bruno, T.J., Lide, D.R. (Eds.), 2015. CRC Handbook of Chemistry and Physics CRC. Press/Taylor and Francis, Boca Raton, FL. Online at. http://www.hbcpnetbase.com/.
Hibiya, K., Terada, A., Tsuneda, S., Hirata, A., 2003. Simultaneous nitrification and denitrification by controlling vertical and horizontal microenvironment in a membrane-aerated biofilm reactor. J. Biotechnol. 100 (1), 23–32.
Hondzo, M., Feyaerts, T., Donovan, R., O'Connor, B.L., 2005. Universal scaling of dissolved oxygen distribution at the sediment-water interface: a power law. Limnol. Oceanogr. 50, 1667–1676.
Jácome, A., Molina, J., Suárez, J., Tejero, I., 2006. Simultaneous removal of organic matter and nitrogen compounds in autoaerated biofilms. J. Environ. Eng. 132 (10), 1255–1263.
Li, J., Zhu, L.P., Xu, Y.Y., Zhu, B.K., 2010. Oxygen transfer characteristics of hydrophilic treated polypropylene hollow fiber membranes for bubbleless aeration. J. Membr. Sci. 362, 47–57.
Martin, K.J., Nerenberg, R., 2012. The membrane biofilm reactor (MBfR) for water and wastewater treatment: principles, applications, and recent developments. Bioresour. Technol. 122, 83–94.
Matsuda, N., Nakamura, M., Sakai, K., Kuwana, K., Tahara, K., 1999. Theoretical and experimental evaluation for blood pressure drop and oxygen transfer rate in outside blood plow membrane oxygenator. J. Chem. Eng. Jpn. 32 (6), 752–759.
Matsumoto, S., Terada, A., Aoi, Y., Tsuneda, S., Alpkvist, E., Picioreanu, C., van Loosdrecht, M.C.M., 2007. Experimental and simulation analysis of community structure of nitrifying bacteria in a membrane-aerated biofilm. Water Sci. Technol. 55 (8–9), 283–290.
Nerenberg, R., 2016. The membrane-biofilm reactor (MBfR) as a counter-diffusional biofilm process. Curr. Opin. Biotechnol. 38, 131–136.
Osa, J., Eguia, E., Vidart, T., Jácome, A., Lorda, I., Amieva, J., Tejero, I., 1997. Wastewater treatment with biofilm membrane reactors. In: Conference on Advanced Wastewater Treatment Processes. Leeds University, Leeds, UK, 1997.
Pankhania, M., Brindle, K., Stephenson, T., 1999. Membrane aeration bioreactors for wastewater treatment: completely mixed and plug-flow operation. Chem. Eng. J. 73 (2), 131–136.
Roggy, D.K., Novak, P.J., Hozalski, R.M., Clapp, L.W., Semmens, M.J., 2002. Membrane gas transfer for groundwater remediation: chemical and biological fouling. Environ. Eng. Sci. 19 (6), 563–574.
Schaffer, R.B., Ludzack, F.J., Ettinger, M.B.C.F.p.d.S., 1960. Sewage treatment by oxygenation through permeable plastic films. J. (Water Pollut. Control Fed. 32 (9), 939–941.
Semmens, M.J., 2008. Alternative MBR configurations: using membranes for gas transfer. Desalination 231 (1), 236–242.
Semmens, M.J., Dahm, K., Shanahan, J., Christianson, A., 2003. COD and nitrogen removal by biofilms growing on gas permeable membranes. Water Res. 37 (18), 4343–4350.
Shi, Y., Hu, S., Lou, J., Lu, P., Keller, J., Yuan, Z., 2013. Nitrogen removal from wastewater by coupling anammox and methane-dependent denitrification in a membrane biofilm reactor. Environ. Sci. Technol. 2013 (47), 11577–11583.
Syron, E., Casey, E., 2008. Membrane-aerated biofilms for high rate biotreatment: performance appraisal, engineering principles, scale-up, and development requirements. Environ. Sci. Technol. 42 (6), 1833–1844.
Tanishita, K., Nakano, K., Sakurai, Y., Hosokawa, T., Richardson, P.D., Galletti, P.M., 1978. Compact oxygenator design with curved tubes wound in weaving patterns. Trans. Am. Soc. Artif. Intern. Organs 24, 327–331.
Terada, A., Hibiya, K., Nagai, J., Tsuneda, S., Hirata, A., 2003. Nitrogen removal characteristics and biofilm analysis of a membrane-aerated biofilm reactor applicable to high-strength nitrogenous wastewater treatment. J. Biosci. Bioeng. 95 (2), 170–178.
Timberlake, D.L., Strand, S.E., Williamson, K.J., 1988. Combined aerobic heterotrophic oxidation, nitrification and denitrification in a permeable-support biofilm. Water Res. 22 (12), 1513–1517.
Weiss, P.T., Gulliver, J.S., Semmens, M.J., 1998. In-stream hollow-fiber membrane aeration. J. Hydraul. Eng. 124 (6), 579–588.
Weissman, M.H., Mockros, L.F., 1969. Oxygen and carbon dioxide transfer in membrane oxygenators. Med. Biol. Eng. 7 (2), 169–184.